


High-Precision Calibration of Phase-Only Spatial Light Modulators

Yicheng Zhao, Wenxiang Yan, Yuan Gao, Zheng Yuan, Zhi-Cheng Ren, Xi-Lin Wang, Jianping Ding , and Hui-Tian Wang

Abstract—In the fields of optics and photonics, phase-only spatial light modulators (SLMs) play an increasingly important role in wave-front engineering. However, the SLMs are subject to wave-front distortion arising from the imperfection in the birefringence effect and physical structure of modulators. This paper presents a simple self-interference phase calibration method applicable to liquid-crystal SLM. We build an interferometric imaging system based on the Pancharatnam phase-shifting to measure the phase distribution of a light beam coming from SLMs. Two types of phase modulation errors of SLMs can be characterized in the measurement process: the erroneous gamma curve and shape aberration. The former belongs to dynamic phase distortion and is measured through a four-step Pancharatnam phase-shifting interference, which allows a one-shot recording of interference pattern via a polarization camera; the latter represents static phase distortion and is extracted from the interference between light waves coming from different regions of the SLM panel by using Zernike polynomial fitting. Our method has the advantages of high-precision pixel-wise phase correction and robustness against environmental disturbance and thus can facilitate the applications of SLM in optical field manipulation.

Index Terms—Spatial light modulator, calibration, phase modulation, interferometer.

I. INTRODUCTION

AS A DYNAMIC and programmable optical element, the liquid crystal spatial light modulator (LC-SLM) has been playing a very important role in the application of wavefront shaping and beam steering. A typical phase-only SLM modulates the wavefront by inducing phase retardance at each liquid crystal pixel, which is controlled by the voltage across the pixel. The corresponding voltage in each pixel is addressed with a computer-loaded grayscale bitmap. It is applied to many fields such as optical microscopy [1], quantum optics [2], [3], optical micro-manipulation [4], [5], holographic display [6], [7], optical coherence tomography [8]. In the applications employing SLMs, high precision light modulation is always desired. However,

normally a commercial SLM suffers from phase distortion. The phase distortion is mainly caused by the phase modulation nonlinearity and non-uniformity of SLM's physical structure and environmental conditions, and can be ascribed to two factors: (1) the erroneous driving electric signal exerted on the liquid crystal (LC) [9] and (2) the backplane curvature and/or thickness variation of the LC layer in SLMs [10]. The former leads to dynamic phase response errors, while the latter results in static wavefront aberrations. To meet the requirement of high-precision wavefront controlling in practical applications, a variety of calibration schemes for compensating the phase distortion have been developed, which are mainly based on three types of measuring principles: interferometry [11]–[14], diffraction technique [15]–[18] and polarimetry [19]–[21]. The three schemes have their pros and cons: interferometric methods are appreciated as the high-precision measurement but are susceptible to environmental vibration; diffraction methods are robust against environmental disturbance but cannot afford spatially varying phase modulation measurement, thereby lacking the ability of pixel-wise calibration; polarization measurement can characterize electro-optic birefringence property of the LC, but the phase estimation operation via birefringence-based optical modeling is a rather complicated process and is usually challenging to achieve pixel-wise phase measurement. In addition, most of the prior literature dealt with severally voltage-phase response calibration or surface compensation, but reports of modulation correction accounting for both voltage-phase mismatch and surface inhomogeneity are scarce.

Considering the above-mentioned concerns, we design and establish an experimental optical system based on self-referencing interference to implement high-precision phase calibration of phase-only SLMs. In the self-reference optical path we designed, the reference light and modulated light come from the same source point and traverse the same path. This arrangement enables the phase measurement to be immune to environmental vibration and can allow the low spatial coherent illumination, which is preferable for suppressing speckle noises. Our phase-correction scheme aims at accomplishing two tasks: phase-voltage gamma curve calibration and surface shape correction. In the gamma correction process, the modulation phase of SLMs is measured through a four-step Pancharatnam phase-shifting interference, which allows a one-shot recording of interference pattern via a polarization camera. In the surface evaluation process, the topographical information of SLMs is extracted from the phase difference between different regions of the SLM

Manuscript received October 22, 2021; revised November 12, 2021; accepted November 15, 2021. Date of publication November 22, 2021; date of current version December 2, 2021. This work was supported in part by the National Science Foundation of China under Grants 91750202 and 11922406, in part by the National Key R&D Program of China under Grants 2018YFA0306200 and 2017YFA0303700. (Corresponding author: Jianping Ding.)

The authors are with the National Laboratory of Solid State Microstructures and School of Physics, Nanjing University, Nanjing 210093, China (e-mail: zycniju@163.com; benson_yan_scut@qq.com; 707848936@qq.com; yuanzheng945945@163.com; zeren@nju.edu.cn; xilinwang@nju.edu.cn; jpdj@nju.edu.cn; htwang@nju.edu.cn).

Digital Object Identifier 10.1109/JPHOT.2021.3129082

panel, and aberration fitting in terms of Zernike polynomials is exploited to retrieve the curvature of SLM. The proposed technique holds promise in three aspects: (1) pixel-wise voltage-phase calibration through a microscopy-based interferometric measuring arrangement; (2) high-precision static surface compensation via Zernike polynomials fitting; (3) robustness against environmental disturbance due to its self-interference character and common-path arrangement.

The outline of this paper is as follows. Section II describes the self-interference principles of the gamma curve correction and the surface measurement of the SLM, along with the corrected phase modulation. Section III shows the experimental comparison results of beam shaping via the SLM that is w/ and w/o phase calibration. Section IV gives the conclusion and final remarks.

II. OPTICAL ARRANGEMENT AND MEASUREMENT PRINCIPLE

To begin with, let us outline the working principle of a reflective phase-only SLM, which is currently the mainstream product widely used for the dynamic engineering of the wavefront. The structure of SLM is a sandwich layer filled with parallel nematic liquid crystals between a glass cover plate and a silicon backplane [22]. The cover plate is coated with a layer of transparent conducting film acting as the common electrode, while the silicon backplane has millions of individually addressable reflective electrode pixels. After an incident light reflects off the SLM, its wavefront will experience pixel-wise phase retardance, which is controlled by the voltage applied across the liquid crystal pixel. The corresponding voltage in each pixel is addressed with a computer-loaded grayscale bitmap, i.e., a computer-generated hologram (CGH), which is produced according to a phase-voltage look-up table (LUT). Ideally, SLM should linearly and pixelated respond to the loaded grayscale map and afford a phase modulation within the range of $0-2\pi$ for a given illumination wavelength. For this purpose, the high precision phase calibration of SLM is required because a commercial SLM generally has a nonlinear and spatially varying phase response. Our proposed phase-correction scheme for the phase-only SLM includes two steps, i.e., (A) phase-voltage gamma curve calibration and (B) surface shape correction, which is performed in a constructed experimental system schematically outlined in Fig. 1 and the underlying working principle will be elaborated in what follows.

A. Gamma Curve Correction

Fig. 1 shows the schematic of our proposed SLM calibration system, which consists of an illumination unit and a measurement unit. In the illumination unit, a laser is used as an illumination source with a wavelength of 532 nm. A rotating ground glass (GG) destroys the spatial coherence of light to reduce speckle noise. The lens L2 can be moved along the optic axis to alter the size of the light spot impinged on the rotating GG, producing an adjustable spatial coherence. After passing through a polarizer P, the light becomes linearly polarized along 45° with respect to the x -direction. The illumination unit is followed by one of two types of measurement units, i.e., (A) Gamma correction unit, and (B) Shape measurement unit.

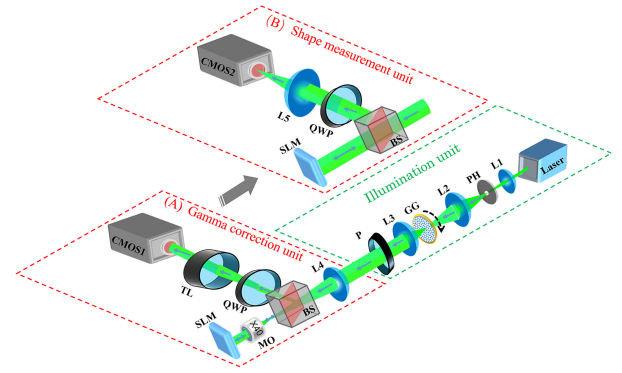


Fig. 1. Outline of measurement optical path. L: lens ($L1 = 250$ mm; $L2 = 50$ mm; $L3 = 200$ mm; $L4 = 70$ mm, $L5 = 200$ mm); PH: pinhole; GG: ground glass; P: polarizer; BS: non-polarizing beam splitter; QWP: quarter-wave plate; TL: tube lens; MO: microscope objective ($\times 40$, $NA = 0.25$); SLM: spatial light modulator. Two kinds of CMOS (complementary metal-oxide-semiconductor) cameras are used. CMOS1 in (A) gamma correction unit: polarization camera (Lucid PHX050S-P, resolution 2448×2048 , pixel pitch $3.45 \mu\text{m}$); CMOS2 in (B) shape measurement unit: CMOS camera (Hamamatsu C11440-36U, resolution 1920×1200 , pixel pitch $5.86 \mu\text{m}$).

In the gamma correction unit, the combination of a microscope objective (MO) and a tube lens (TL) establishes a microscopic imaging relation between the SLM under test and the camera plane; the reflected light off the SLM, which is composed of the x - and y -polarized components, is collected by the MO and imaged on a polarization camera. Owing to the modulation character of the phase-only SLM, the x -polarized component is phase-modulated while the phase of the y -polarized one remains unchanged after reflecting from the SLM. The two linear components are converted into mutually orthogonal circular polarizations via a quarter-wave plate (QWP) with its fast axis orientating at 45° with respect to the x -direction and interfering with each other on the camera plane. The use of high-quality MO allows the high spatially resolved interferometric images to be formed in the camera. Note that both the x - and y -polarized components come from the single linearly polarized light beam impinging on the same place of the SLM, thereby implying that the superposition of the two waves resembles a self-referencing interference.

The extraction of the modulation phase from the interference pattern recorded by the camera is based on the well-known phase-shifting interferometry. Our phase-evaluation method utilizes the polarization state of light to realize the so-called Pancharatnam phase-shifting [23]. When a linearly polarized light illuminates the SLM, the x -polarized component of the reflected light acquires a phase-only modulation, while the y -polarized component reflecting off the SLM does not undergo modulation, and hereby acts as the reference wave. The QWP converts the x - and y -polarized components into the left- and right-hand circularly-polarized components, respectively. After passing through a polarizer with its transmission axis orientating at an angle θ with respect to the x -direction, the Pancharatnam-phase-stepped intensity distributions can be recorded by the camera, which has the following expression [24]

$$I(\theta) = \frac{1}{2} [I_x + I_y + 2\sqrt{I_x I_y} \cos(\phi + 2\theta)], \quad (1)$$

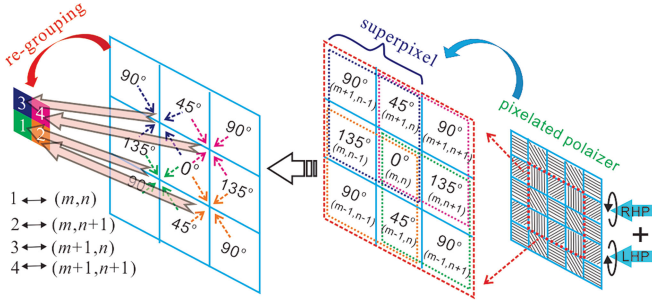


Fig. 2. Principle of four-step spatial Pancharatnam-phase shift via the single-shot recording of interference between the left-hand polarized (LHP) signal wave and the tight-hand polarized (RHP) reference wave. Four adjacent micropolarizers with four discrete polarizations at 0, 45, 90, and 135 degrees are combined to form a superpixel for the four-step phase-shifting algorithm and are re-grouped through spatial pixel multiplexing to restore the spatial resolution.

where $\phi = \phi_x - \phi_y$, ϕ_x is the phase that SLM modulates, ϕ_y is a constant because SLM does not modulate the phase of the y -polarized component, and therefore ϕ is equivalent to ϕ_x . I_x and I_y are the intensities of the x and y polarization components, respectively. The argument 2θ is the so-called geometrical (Pancharatnam) phase. In the above expression, we have implied but suppressed the dependence of the quantities on the spatial coordinate (x, y) for brevity. According to the four-step phase-shifting algorithm [25], we can retrieve the phase ϕ as

$$\phi = \arctan \left[\frac{I(135^\circ) - I(45^\circ)}{I(0^\circ) - I(90^\circ)} \right]. \quad (2)$$

Normally a multi-step phase-shifting requires a sequentially multiple recording of the interference pattern and is thus unable to achieve instantaneous interferometric measurements. By contrast, our measurement system allows a one-shot phase-shifting interference through the combination of a polarization camera with the spatial Pancharatnam-phase shift. A polarization camera incorporates a micropolarizer array in front of the camera sensor by means of matching the size of the pixelated linear polarizer with that of the detector [26]. Four micropolarizers with four discrete polarization (0, 45, 90, 135 degrees) are adjacent to each other and are combined to form a superpixel, whose concept is schematically shown in Fig. 2, enabling a single-shot recording of the four-step phase-shifted interferogram. Such a superpixel is repeated continuously over the entire detector array. The resolution of the superpixel is seemingly reduced to half of that of the native sensor. However, we can regroup superpixels via spatial pixel multiplexing to recover the resolution, as illustrated in Fig. 2. For example, the pixel at (m, n) will be re-combined with its three adjacent pixels at $\{(m, n-1), (m-1, n-1), (m-1, n)\}$ to form a new pixel numbered by (m, n) . In this way, the wavefront phase to be measured can be extracted with an almost full resolution at native sensor pixels through the above-described polarization phase-shifting interferometric measurement. The dimension of the measured phase data differs inappreciably from that of the detector array, for instance, an $M \times N$ sensor array will give rise to a measured phase data of $(M-1) \times (N-1)$. It should be pointed out that a similar gamma correction based on the polarization phase-shifting has been reported in our previous work [24], wherein, however, the four

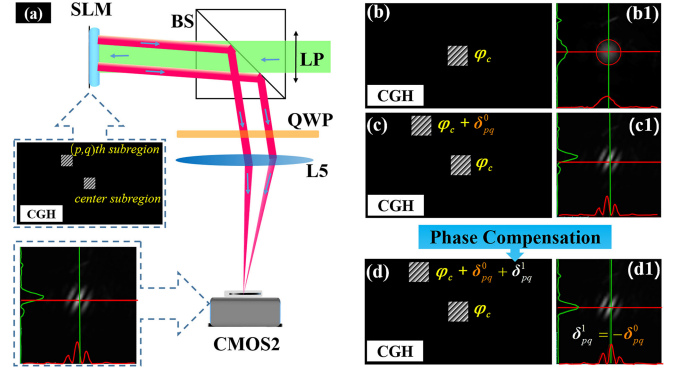


Fig. 3. Off-axis light path diagram (a) and more detailed illustration (b)-(d). (a): LP: linear polarization; BS: beam splitter; SLM: spatial light modulator; L5: lens ($L5 = 200\text{mm}$); CMOS2: (Hamamatsu C11440-36U, resolution 1920×1200 , pixel pitch $5.86 \mu\text{m}$). (b)-(d): (b) only open the center region to determine the reference point shown in (b1). (c) open subregion (i, j) to determine the deviation. (d) compensation deviation.

frames of interferograms were recorded sequentially in four steps.

Ideally, the phase modulation of an 8-bit SLM should produce a linear 2π phase distribution overall gray levels within $[0, 255]$. Unfortunately, this is rarely the case for a practical SLM, which should be calibrated for high-precision phase manipulations. Here we leverage the above-introduced phase measurement system to precisely calibrate the phase modulation of SLM. By taking advantage of high spatially resolved microscopic imaging, we carry out pixel-wise gamma value calibration by measuring the phase response to the different gray-level patterns. The relevant results will be presented in Section III.

B. Shape Aberration Correction

When the electrical driving signal is switched off, an ideal SLM should act as a flat mirror. In practice, however, the backplane curvature and/or thickness variation of the LC layer in commercial SLMs will result in the phase distortion of the light wavefront to be modulated. In other words, the phase of reflected light varies from place to place across the panel of the SLM illuminated by a collimated light. This modulation error is a static error and must be corrected when applying the SLM in high-precision modulation of light waves. For compensating for the modulation error due to the SLM surface curvature or any aberrations in the optical train before or after the SLM panel, we need to measure the topographical distribution of the SLM panel. This characterizing task is implemented by the shape measurement unit shown in Fig. 1. Since a constant or piston phase delay in the wavefront does not have any practical interest, the relative shape topography of the SLM is what we are concerned with. Hence we choose the center region of the SLM as the reference and evaluate the phase difference of two light waves which are reflected from the center region and the other location on the SLM panel, respectively.

Fig. 3 schematically outlines the principle of the proposed shape measurement method. The entire panel of the SLM under test is evenly divided into a set of subregions, say $P \times Q$ subregions, each of which is square and is independently loaded with

a blazed grating pattern. Accordingly, the entire reflected beam from the SLM can be seen as a series of beamlets distributed as a rectangular lattice on the SLM plane, and the reflected beamlet from a subregion can be directed to the first or zeroth diffraction order depending on the respective blazed grating is turned on or off. In the shape measurement, we choose only two subregions of the SLM panel to be loaded by respective blazed grating patterns; one subregion is at the center place of the SLM and the other subregion, say the (p, q) th subregion, located at a place to be evaluated. An x -polarized light illuminates the SLM and produces the first-order diffracting light on the detection window of the camera. After being focused by a lens (L5 shown in Fig. 3(a)), only two first-order light waves from two different subregions will interfere with each other. If the SLM has no shape distortion, two beamlets diffracted from two different subregions with the identical blazed grating will have the same phase and thus yield a constructive interference. Therefore, we can characterize the shape variation of the SLM by monitoring the intensity at the center of the first-order spot.

Figs. 3(b)–(d) illustrate the procedure of our proposed surface evaluation in more detail. First, only the center area is opened, and the center of the first-order light spot, marked by the cross-point shown in Fig. 3(b1), has a maximal intensity and is taken as the calibration point. Then, as shown in Fig. 3(c), the (p, q) th subregion to be evaluated is opened so that the first-order light from this subregion can interfere with that from the central region, resulting in the interference pattern shown in Fig. 3(c1). The intensity at the calibration point is related to the phase difference, δ_{pq}^0 , between the two interfering waves. This phase difference δ_{pq}^0 also represents the shape distortion at the (p, q) th subregion relative to the center of the SLM panel. As shown in Fig. 3(d), tuning a phase shift, δ_{pq}^1 , of the blazed grating pattern loaded on the (p, q) th subregion will alter the intensity at the calibration point. When $\delta_{pq}^1 = -\delta_{pq}^0$ the calibration point will reach an intensity maximum, as shown in Fig. 3(d1), and thus the shape distortion at the (p, q) th subregion is determined. In this way, the shape curvature of the entire SLM panel can be characterized.

The above-acquired shape information on the set of $P \times Q$ locations represents an under-sampled phase map compared with the original dimension of the SLM. To retrieve the pixel-wise curvature of the entire SLM we propose to employ Zernike-polynomial fitting for the under-sampled curvature distribution. For this purpose, we write the measured curvature on the two-dimensional Cartesian grid of $P \times Q$, $W(x_p, y_q) = \delta_{pq}^0$, as the Zernike-polynomial expansions according to [25]

$$W(x_p, y_q) = \sum_{j=1}^J a_j Z_j(x_p, y_q) \quad (3)$$

where $Z_j(x_p, y_q)$ is the j -th Zernike polynomial and J is the number of Zernike polynomials chosen for expansions. a_j is the Zernike coefficient, which can be calculated as below

$$a_j = \frac{\sum_{p=1}^P \sum_{q=1}^Q W(x_p, y_q) Z_j(x_p, y_q)}{\sum_{p=1}^P \sum_{q=1}^Q Z_j^2(x_p, y_q)}. \quad (4)$$

Once Zernike coefficients are determined, we can reconstruct the full-resolution distribution of curvature by replacing the subregion location with the pixel location on the SLM panel in the Zernike-polynomial expansions of Eq. (3). This interpolation practice is effective because normally the shape curvature of commercial SLMs varies continuously from pixel to pixel.

III. EXPERIMENTAL CALIBRATION AND VERIFICATION RESULTS

The modulation calibration of the SLM under test is carried out according to the procedure schematically illustrated in Fig. 4, which includes two steps –(A)the gamma correction and (B) the shape correction. The manufacturer has provided the original gamma curve of the gray level vs. an intermediate parameter, namely lookup table (LUT) value, which is proportional to the voltage across the LC cell. Such a LUT is calibrated in the gamma correction. From the measured phase-gray curve we first correct the relation of LUT vs. gray level (gamma curve) and then calibrate the phase modulation against the grayscale. In the subsequent shape correction procedure, the shape distribution of the SLM is measured and the phase compensation needed for correcting the shape error is determined. Finally, the dynamic grayscale-to-phase modulation error and the static shape error of the SLM will be jointly compensated when applying the SLM to modulate a light wave to be manipulated. In our optical system, high-quality lenses are used for assuring that the possible lens aberration is eliminated.

A. Results of Gamma Curve Correction

Using the above-described method, we have measured the phase-gray relation of a phase-only SLM (Holoeye Leto, resolution 1920×1080 , pixel pitch $6.6 \mu\text{m}$) under the illumination of the light wavelength of 532 nm. On the SLM's pixel to be tested we sequentially load the prepared gray patterns with their gray level successively varying from 0 to 255. The ideal phase modulation of SLM should produce a linear 2π phase distribution overall gray levels within $[0, 255]$, but this is rarely the case for current commercial SLMs. Fig. 5(a) shows the measured phase modulation vs. gray level, corresponding to three zones (marked by 1, 2, and 3 in the inset of Fig. 5(a)) in the panel of the SLM under test. Zones 1, 2, and 3 represent three typical regions at the corner, edge, and center of the SLM, respectively, each of which has an 8×8 array of pixels. The measured results in Fig. 5(a) demonstrate that the actual phase modulation obtained from the manufacturer's gamma curve indeed deviates from the ideal (theoretical) phase-gray curve. Furthermore, the difference in the three curves clearly indicates the spatial nonuniformity of phase modulation over the entire panel of SLM, i.e., different pixels of the SLM have different phase modulation outputs. This spatial nonuniformity is in contrast to the common assumption that commercial phase-only SLMs have the same phase modulation property for all the pixels. Our calibration method enables a pixel-wise measurement and correction of the phase-gray curve. As a representative example, Fig. 5(b) shows the corrected phase-gray curve responsible for zone 3, which agrees very well with the theoretical curve. Besides, the

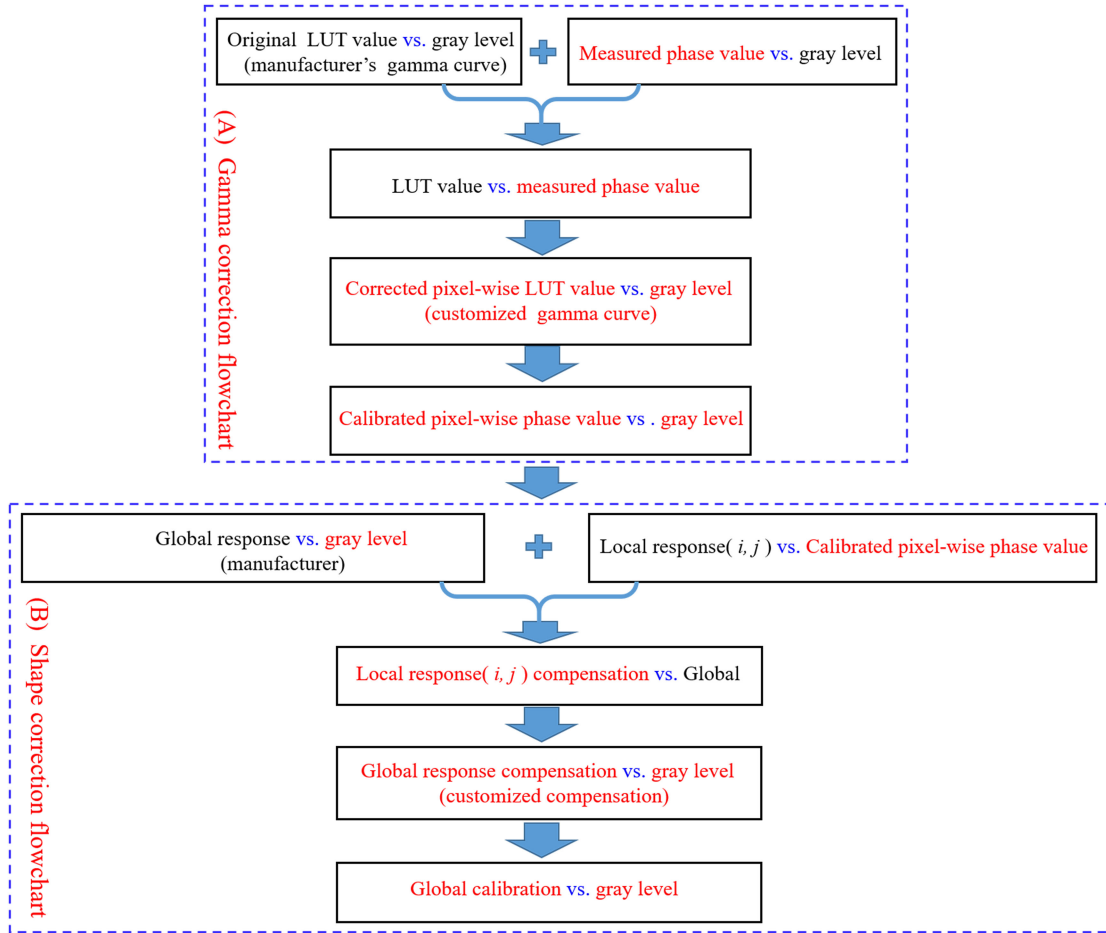


Fig. 4. Flowchart of the calibration procedure. (a) Gamma correction flowchart (b) Shape correction flowchart.

calibration performance is also confirmed by the error curve before and after the calibration shown in Fig. 5(b).

Once we finish the gamma curve correction, we move on to the next step — characterizing the shape topography of the SLM, as will be demonstrated in the next subsection.

B. Results of Shape Curvature Correction

For the shape correction of SLM, we need to select the appropriate subregion size to load the grazed grating pattern. The larger the subregion, the lower the spatial resolution of shape measurement. However, if the subregion is too small, the number of grating cycles is limited, which will impair the phase controlling accuracy of first-order diffracting light. As the surface aberrations in a commercial SLM are smooth functions with very low spatial frequencies, we find that a subregion size with 21×21 pixels is a proper choice for the SLM under test. Setting the subregion size to be 21×21 pixels rather than 8×8 pixels chosen in the gamma correction allows more periods of grating pattern to be displayed on the SLM while still guaranteeing the spatial resolution of shape measurement. Accordingly, the number of subregions becomes 90×49 . Following the measurement principle described in Section II(B), we measure the shape-associated phase distribution, $W(x_p, y_q)$ in Eq. (3),

that is a sampled data at the two-dimensional grid of 90×49 . Based on these measured phase data, we calculate out Zernike fitting coefficients according to Eq. (4) and further interpolate the shape curvature across the pixel array of 1920×1080 . The reconstructed phase aberration is shown in Fig. 6. The root-mean-square (RMS) and peak-to-valley (PV) of the surface aberration are measured to be 0.288λ and 0.049λ , respectively, with λ being the wavelength of the illumination light. In our case, the first 36 Zernike polynomials are sufficient for fitting the aberration of the SLM to be tested. Besides, the first, second, and third Zernike polynomials represent the piston, x tilt, and y tilt, respectively, which are not concerned with. Hence we give the measured Zernike coefficients with index from 4 to 36 in Fig. 7.

C. Performance of Corrected SLM on Generating Special Light Beams

To demonstrate the utility of our calibration method, we apply the phase-only SLM under test (Holoeye Leto) to generate some special beams and compare the modulation effect of the SLM before and after calibration. We test the SLM by loading on it the phase-only CGH that can produce the desired complex field in the focal space. The first demonstration example is the

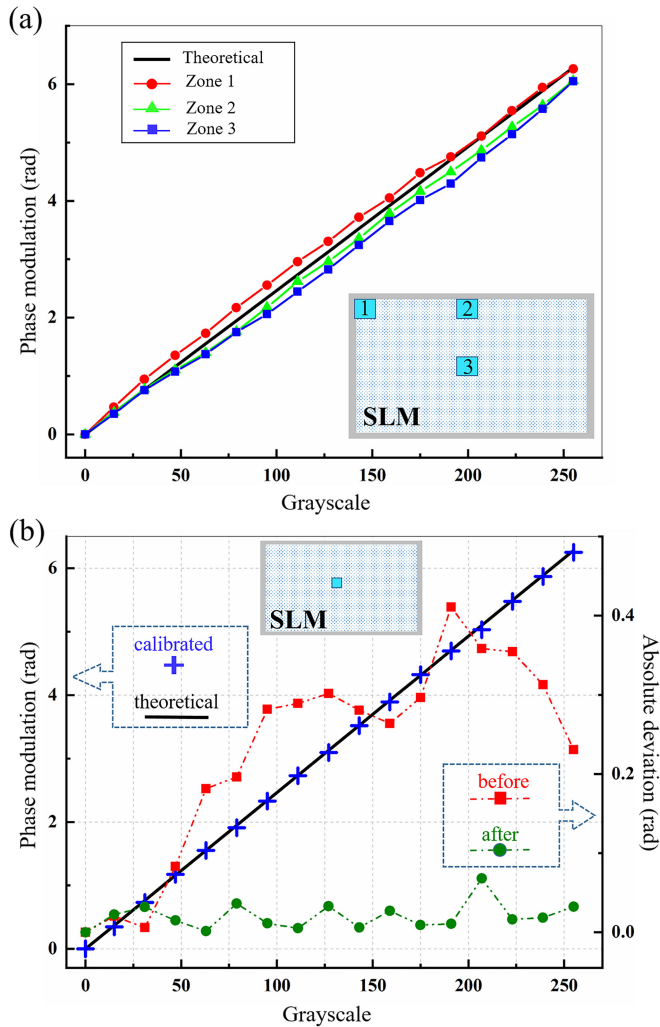


Fig. 5. Gamma curve (phase-grayscale relation) of the SLM under test. (a) Measured gamma curve in three regions of the SLM panel. (b) Calibrated gamma curve of the center region and error comparison between before and after phase modulation calibration.

vortex beam having a spiral phase represented by $\exp(il\varphi)$, with φ being the azimuthal coordinate and l denoting topological charges of the vortex phase. We use the same optical path as the shape measurement unit in Fig. 1 to observe the focal field of the SLM-generated vortex beams. The resulting field is recorded by a camera in the focal plane of the lens (L5) with a focal length of 200 mm. Considering the cylindrical symmetry of the vortex beams, we use a circular area on the SLM panel to load the CGH. As shown in the left panels in Figs. 8(a)–(c), three regions located at the left to the right on the SLM panel, denoted by S1, S2, and S3, are imprinted by the CGH pattern responsible for vortex beams with topological charges of 1 to 5. Each circular-shaped CGH has a diameter of 900 pixels. The vortex beam generated from the SLM under default settings of the manufacturer and after calibration is captured and shown in Fig. 8. As seen in Fig. 8, before calibration, the bright focal ring of the vortex beam turns out to be asymmetry, which becomes even acute for lower topological charges. By contrast, the quality of the light field is significantly improved after the SLM is calibrated

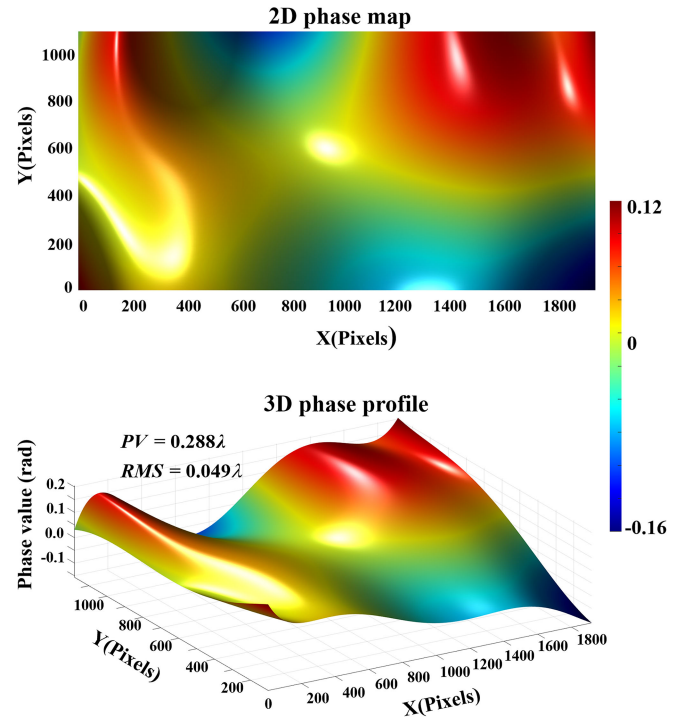


Fig. 6. Two-dimensional phase distribution (top) and three-dimensional phase profile of the measured phase distortion due to the shape aberration of the SLM under test.

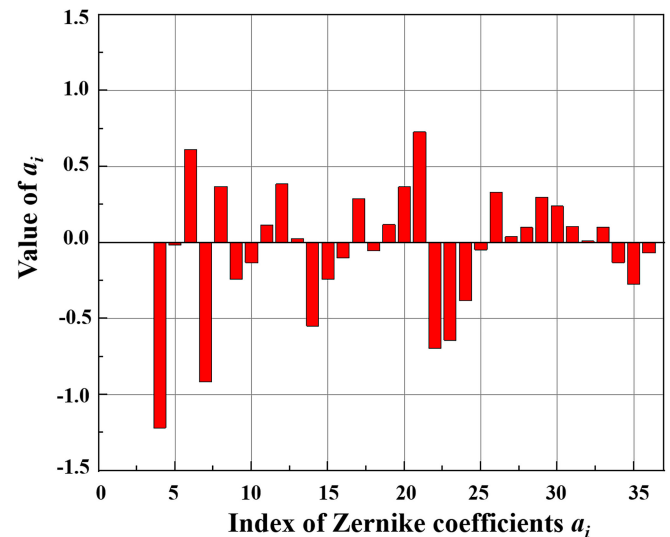


Fig. 7. Measured Zernike coefficients a_i with $i = 4, 5, \dots, 36$.

using our method. This result also indicates that different region of the SLM has different phase modulation behavior, and thus confirms the necessity of the local modulation calibration from place to place can greatly when high-precision modulation is highly desired.

In order further to illustrate the calibration accuracy, we use the SLM to generate modified Bessel beams (BBs) with an on-demand tailored intensity along the z-axis [27]. The angular spectrum of the desired BBs can be expressed in the cylindrical

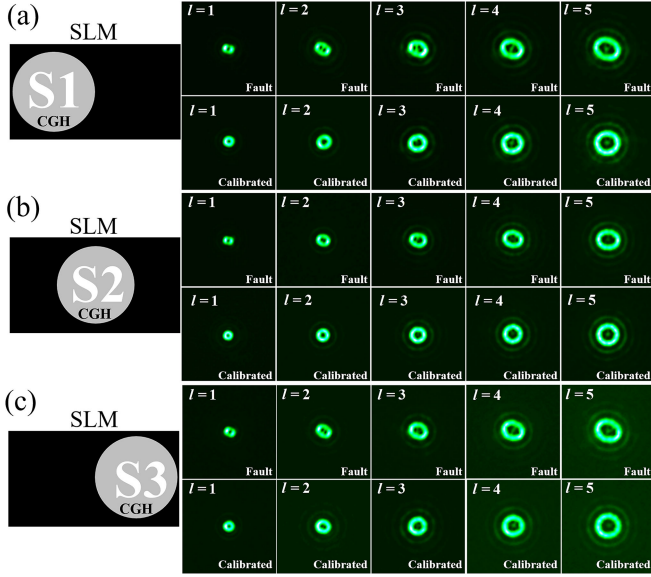


Fig. 8. Focal field intensity produced from vortex phase CGHs loaded on three different regions, (S1, S2, S3), of the SLM. Five vortex beams with their topological charge $l = 1, 2, 3, 4,$ and 5 are generated for comparing the phase modulation performance of the SLM with fault and calibrated gamma curves.

coordinates (k_r, θ, k_z) by

$$A \left(k_r = \sqrt{k^2 - k_z^2}, \theta, k_z \right) = \frac{2e^{i\theta}}{\text{rect} \left(\frac{k_z}{2k} \right) k_z} \int_{-\infty}^{\infty} \sqrt{I(z)} e^{-ik_{z0}z} e^{-ik_z z} dz, \quad (5)$$

where $k = 2\pi/\lambda$ is the wavenumber and k_{z0} is a specified longitudinal wave vector of the BBs. Eq. (4) $\text{rect}(\cdot)$ represents the rectangle function and $I(z)$ is the desired intensity distribution along the z -direction. In this demonstration case, we set $I(z) = 1$ and $k_{z0} = 0.99994k$. This arrangement can enable the generated BBs to hold non-diffracting within a range of 30 mm before and after the focal plane. Of course, we can design a longer non-diffraction distance. The reader can refer to [27] for more properties of such BBs. We apply the cosine-modulation encoding method to generate the phase-only CGH that can reconstruct the desired complex field. Fig. 9 presents two generated BBs with topological charges of $l = 1$ and $l = 3$, showing the propagation behavior of the modified BBs with non-diffraction and longitudinal intensity customizability. The generated CGH is loaded on the center region of the SLM. Four kinds of designed BBs are shown in Fig. 9 for comparison: (1) the theoretical beam, (2) the beam generated by the SLM under fault setting, (3) the beam generated by the SLM with gamma calibration, and (4) the beam generated by the SLM with both gamma calibration and shape correction. Better visualization of beam quality can be obtained from the two-dimensional distribution in the focal plane, as shown in the inset of Fig. 9. Fig. 9 shows that the SLM with both gamma calibration and shape correction can provide the highest modulation quality. Besides, this comparison implies that for the SLM under test the shape correction plays the most important role in improving the reconstruction quality of designed fields.

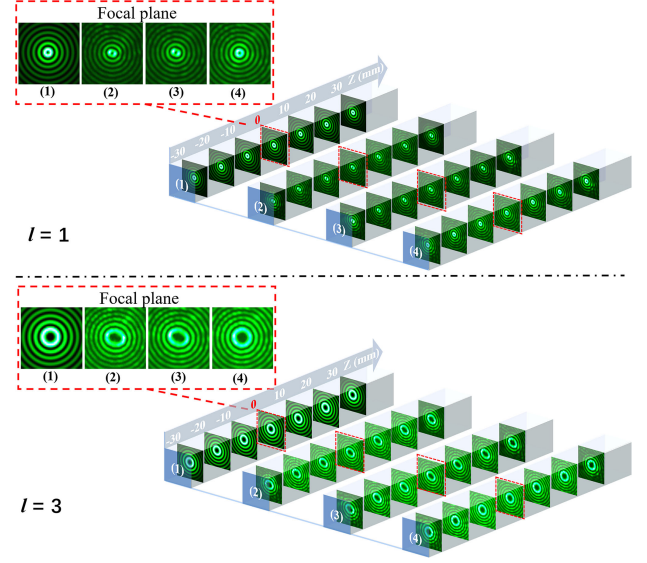


Fig. 9. Cross-sectional intensity map of generated BBs propagating along the z -direction. Four BBs are generated by (1) the theory, (2) the SLM under fault setting, (3) the SLM with gamma calibration, and (4) the SLM with both gamma calibration and shape correction. Top: topological charge $l = 1$; bottom: topological charge $l = 3$.

IV. CONCLUSION

Phase-only SLMs are becoming the ever-increasingly preferred devices for light steering, and thus the SLM's phase modulation calibration becomes highly demanded in high-precision applications. In this work, we propose a self-referencing-interference based on the pixel-wise phase calibration method. The phase modulation of individual pixels on SLM can be assessed and calibrated with high accuracy through specially designed interferometric microscopy, which can measure the modulated phase through a one-shot recording of four-step Pancharatnam phase-shifting interference. Furthermore, the shape aberration can be measured and corrected in our experimental system. Owing to the self-referencing and common-path optical arrangement, our method shows advantages of good stability against environmental disturbance and high reliability for quantitative phase measurement. Since there commonly exists modulation nonuniformity across the SLM panel, we believe that the proposed pixel-wise calibration technique is very helpful for both SLM users aiming at the high-quality controlling of light and manufacturers for their product testing and evaluation.

REFERENCES

- [1] C. Maurer, A. Jesacher, S. Bernet, and M. Ritsch-Marte, "What spatial light modulators can do for optical microscopy," *Laser Photon. Rev.*, vol. 5, no. 1, pp. 81–101, Jan. 2011.
- [2] J. Leach *et al.*, "Quantum correlations in optical angle-orbital angular momentum variables," *Science*, vol. 329, no. 5992, pp. 662–665, Aug. 2010.
- [3] A. Lubatsch and R. Frank, "Evolution of Floquet topological quantum states in driven semiconductors," *Eur. Phys. J. B*, vol. 92, no. 9, Sep. 2019, Art no. 92215..
- [4] D. G. Grier, "A revolution in optical manipulation," *Nature*, vol. 424, no. 6950, pp. 810–816, Aug. 2003.
- [5] A. Lizana *et al.*, "Generation of reconfigurable optical traps for microparticles spatial manipulation through dynamic split lens inspired light structures," *Sci. Rep.*, vol. 8, no. 1, Dec. 2018, Art. no. 11263.

- [6] Z. He, X. Sui, G. Jin, D. Chu, and L. Cao, "Optimal quantization for amplitude and phase in computergenerated holography," *Opt. Exp.*, vol. 29, no. 1, p. 119–133, Jan. 2021.
- [7] J. Christmas and N. Collings, "Displays based on dynamic phase-only holography," *Appl. Sci.*, vol. 8, no. 5, Apr. 2018, Art. no. 685.
- [8] C. Park, K. Lee, Y. Baek, and Y. Park, "Low-coherence optical diffraction tomography using a ferroelectric liquid crystal spatial light modulator," *Opt. Exp.*, vol. 28, no. 26, Dec. 2020, Art. no. 39649.
- [9] D. Engström, M. Persson, J. Bengtsson, and M. Goksör, "Calibration of spatial light modulators suffering from spatially varying phase response," *Opt. Exp.*, vol. 21, no. 13, Jul. 2013, Art. no. 16086.
- [10] J. B. Bentley, J. A. Davis, J. Albero, and I. Moreno, "Self-interferometric technique for visualization of phase patterns encoded onto a liquid-crystal display," *Appl. Opt.*, vol. 45, no. 30, Oct. 2006, Art. no. 7791.
- [11] H. Zhang, J. Zhang, and L. Wu, "Evaluation of phase-only liquid crystal spatial light modulator for phase modulation performance using a Twyman–Green interferometer," *Meas. Sci. Technol.*, vol. 18, no. 6, pp. 1724–1728, Jun. 2007.
- [12] S. Reichelt, "Spatially resolved phase-response calibration of liquid-crystal-based spatial light modulators," *Appl. Opt.*, vol. 52, no. 12, Apr. 2013, Art. no. 2610.
- [13] F. P. Ferreira and M. S. Belsley, "Direct calibration of a spatial light modulator by lateral shearing interferometry," *Opt. Exp.*, vol. 18, no. 8, Apr. 2010, Art. no. 7899.
- [14] J. L. M. Fuentes, E. J. Fernández, P. M. Prieto, and P. Artal, "Interferometric method for phase calibration in liquid crystal spatial light modulators using a self-generated diffraction-grating," *Opt. Exp.*, vol. 24, no. 13, Jun. 2016, Art. no. 14159.
- [15] L. Martínez-León, Z. Jaroszewicz, A. Kołodziejczyk, V. Durán, E. Tajahuerce, and J. Lancis, "Phase calibration of spatial light modulators by means of Fresnel images," *J. Opt. A: Pure Appl. Opt.*, vol. 11, no. 12, Dec. 2009, Art. no. 125405.
- [16] Z. Zhang *et al.*, "Diffraction based phase compensation method for phase-only liquid crystal on silicon devices in operation," *Appl. Opt.*, vol. 51, no. 17, Jun. 2012, Art. no. 3837.
- [17] O. Mendoza-Yero *et al.*, "Diffraction-based phase calibration of spatial light modulators with binary phase Fresnel lenses," *J. Display Technol.*, vol. 12, no. 10, pp. 1027–1032, Oct. 2016.
- [18] H. Zhang *et al.*, "LCoS display phase self-calibration method based on diffractive lens schemes," *Opt. Lasers Eng.*, vol. 106, pp. 147–154, Jul. 2018.
- [19] J. E. Wolfe and R. A. Chipman, "Polarimetric characterization of liquid-crystal-on-silicon panels," *Appl. Opt.*, vol. 45, no. 8, Mar. 2006, Art. no. 1688.
- [20] F. J. Martínez *et al.*, "Averaged stokes polarimetry applied to evaluate retardance and flicker in PA-LCoS devices," *Opt. Exp.*, vol. 22, no. 12, Jun. 2014, Art. no. 15064.
- [21] A. Márquez *et al.*, "Unitary matrix approach for a precise voltage dependent characterization of reflective liquid crystal devices by average stokes polarimetry," *Opt. Lett.*, vol. 45, no. 20, Oct. 2020, Art. no. 5732.
- [22] R. Li and L. Cao, "Progress in phase calibration for liquid crystal spatial light modulators," *Appl. Sci.*, vol. 9, no. 10, May 2019, Art. no. 2012.
- [23] J. A. Ferrari, E. M. Frins, and W. Dultz, "Optical fiber vibration sensor using (Pancharatnam) phase step interferometry," *J. Lightw. Technol.*, vol. 15, no. 6, pp. 968–971, Jun. 1997.
- [24] J. Xia *et al.*, "Pixel-addressable phase calibration of spatial light modulators: A common-path phase-shifting interferometric microscopy approach," *J. Opt.*, vol. 19, no. 12, Dec. 2017, Art. no. 125701.
- [25] D. Malacara, Ed., *Optical Shop Testing*, 3rd ed. Hoboken, NJ, USA: Wiley-Interscience, 2007.
- [26] N. Brock, B. T. Kimbrough, and J. E. Millerd, "A pixelated micropolarizer-based camera for instantaneous interferometric measurements," in *Proc. SPIE Int. Soc. Opt. Eng.*, San Diego, CA, USA, Sep. 2011, pp. 1–9.
- [27] W. Yan *et al.*, "Non-diffracting and self-accelerating bessel beams with on-demand tailored intensity profiles along arbitrary trajectories," *Opt. Lett.*, vol. 46, no. 7, Apr. 2021, Art. no. 1494.